Article

# $^1$H Detected Relayed Dynamic Nuclear Polarization

Pierrick Berruyer, Andrea Bertarello, Snædís Björgvinsdóttir, Moreno Lelli, and Lyndon Emsley*

Read Online

ACCESS | Metrics & More | Article Recommendations | SI Supporting Information

**ABSTRACT:** Recently, it has been shown that methods based on the dynamics of $^1$H nuclear hyperpolarization in magic angle spinning (MAS) NMR experiments can be used to determine mesoscale structures in complex materials. However, these methods suffer from low sensitivity, especially since they have so far only been feasible with indirect detection of $^1$H polarization through dilute heteronuclei such as $^{13}$C or $^{29}$Si. Here we combine relayed-DNP (R-DNP) with fast MAS using 0.7 mm diameter rotors at 21.2 T. Fast MAS enables direct $^1$H detection to follow hyperpolarization dynamics, leading to an acceleration in experiment times by a factor 16. Furthermore, we show that by varying the MAS rate, and consequently modulating the $^1$H spin diffusion rate, we can record a series of independent R-DNP curves that can be analyzed jointly to provide an accurate determination of domain sizes. This is confirmed here with measurements on microcrystalline L-histidine·HCl·H$_2$O at MAS frequencies up to 60 kHz, where we determine a Weibull distribution of particle sizes centered on a radius of $440 \pm 20$ nm with an order parameter of $k = 2.2$.
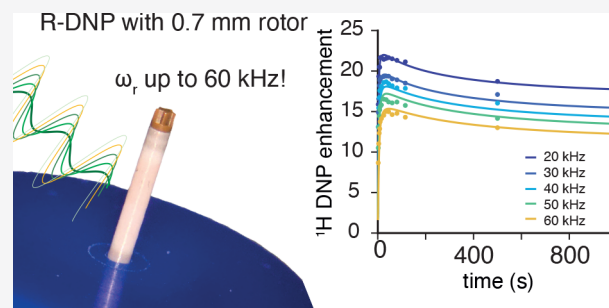
## INTRODUCTION

Modern functional materials such as drug delivery systems,[1,2] formulated pharmaceuticals,[3] energy materials (*e.g.* organic solar cells, batteries, or hybrid perovskites),[4−6] or porous solids[7] are usually multicomponent materials whose interfaces, structural hierarchies, and domain sizes are complex and play an important role in determining the final functional properties. Although many techniques, such as electron microscopy, can provide important insight, there are still many challenges associated with fully determining such aspects in modern materials.

NMR spectroscopy is today well established as a method of choice to determine atomic-level structure and dynamics in complex materials.[8−20] NMR can also be used to reveal longer range aspects of structure.[8,17] In particular, pioneering work by Schmidt-Rohr, Spiess, and co-workers showed that $^1$H spin diffusion is a powerful mechanism that allows to explore sample homogeneity and measure polymer domain sizes.[21−23]

Dynamic nuclear polarization (DNP) under magic angle spinning (MAS) is a hyperpolarization method that relies on the transfer of electron spin polarization to nuclear spins upon microwave ($\mu$wave) irradiation at or near the EPR frequency of the electron spins.[24,25] To achieve this in materials, as shown in Figure 1, the material is typically impregnated with a radical containing solution.[26] Once frozen at ∼100 K, $\mu$wave irradiation induces transfer of polarization from electrons to nearby $^1$H, and finally the hyperpolarization is spontaneously propagated throughout the impregnated material via $^1$H spin diffusion, and then typically transferred to a heteronucleus for observation.[27,28]
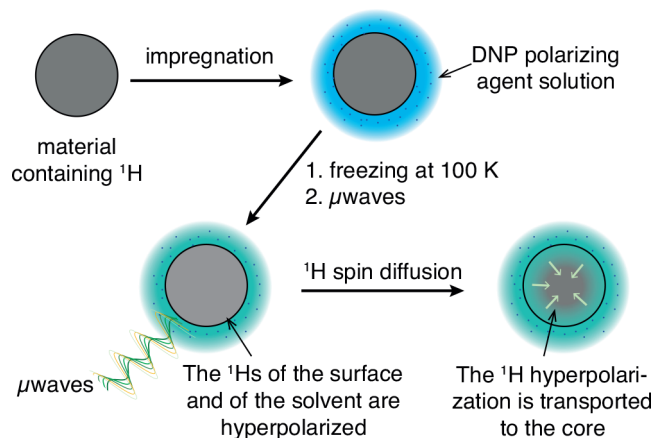


**Figure 1.** Principle of Relayed DNP. A material is impregnated with a solution of a DNP polarizing agent. Once frozen, upon $\mu$wave irradiation, the $^1$H spins in the solvent phase are hyperpolarized. The hyperpolarization then spontaneously diffuses into the bulk material.

Capitalizing on early work by Van Der Wel et al.[28] and Rossini et al.,[27] in 2017 Pinon et al. combined $^1$H spin diffusion with hyperpolarization from DNP and quantitative
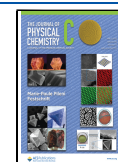
numerical models to measure domain sizes in crystalline powders, mesoporous silica materials, and mixed composition cellulose-based films.[29] The method, denoted Relayed DNP (R-DNP), has since been successfully applied to determine the *de novo* structure of lipid nanoparticles (such as those used to deliver mRNA-based vaccines),[30] changes in the topology of lignins in biomass subjected to extraction,[31] the core–shell structure of organic crystalline drug nanoparticles (CNPs),[32] the presence of an insoluble amorphous form of a drug at the surface of crystalline particles of the salt form,[33] and the spatial distribution of functional groups in cellulose ethers.[34]

Although R-DNP is a powerful method to measure domain sizes, it suffers from low sensitivity. Indeed, while DNP enhanced spectra offer substantial gains in sensitivity, and generally accelerate experiments, the R-DNP approach relies on recording the dynamics of the DNP enhancement as a function of the polarization time, which requires recording signal build-up experiments with and without $\mu$wave irradiation. Typical experimental conditions are at a magnetic field of 9.4 T, with a sample spinning at 8–12.5 kHz, at a temperature of ~100 K, where the $^1$H polarization must be monitored through a transfer experiment to heteronuclei (typically $^{13}$C or $^{29}$Si) to afford spectral differentiation of the sample components. Recording signal build-ups without $\mu$waves often requires days of signal averaging!

In 2020, we reported DNP MAS experiments using 0.7 mm diameter rotors.[35] Such rotors enabled DNP experiments with MAS rates up to 65 kHz, at ~100 K, and under $\mu$wave irradiation. At 21.2 T, DNP enhancements as high as 200 were reported at 65 kHz MAS rates using the HyTEK-2 polarizing agent.[35,36] We also obtained the best $^1$H resolution directly observed in MAS DNP experiments so far. This unprecedented $^1$H resolution enabled the implementation of $^1$H detected $^1$H–$^{13}$C DNP HETCOR experiments.[35]

Here we combine R-DNP with fast MAS (up to 60 kHz) using 0.7 mm diameter rotors at 21.2 T, to follow the hyperpolarization dynamics in a microcrystalline powder of L-histidine·HCl·H$_2$O impregnated with 32 mM HyTEK-2 in 1,1,2,2-tetrachloroethane (TCE). We find that a very significant reduction in experimental times can be achieved by implementing direct $^1$H detection, instead of detection through a heteronucleus, specifically here a reduction in time by a factor of ~16 (by direct comparison of the experimental times reported in ref 29 and here). Furthermore, with this accelerated approach we show that by varying the MAS rate, and consequently modulating the $^1$H spin diffusion rate, we can record a series of independent R-DNP curves that can be analyzed jointly to provide an accurate determination of domain sizes (and spin diffusion coefficients).

## ■ EXPERIMENTAL SECTION

Experiments were carried out on L-histidine·H$_2$O·HCl purchased from Sigma-Aldrich and used without further purification. The as received powder was ground manually with a pestle and mortar for about 15 min to reduce the size of the particles. All samples were prepared using the same batch of ground powder to reduce any potential variability due to impurities or particle size distributions between samples.

For DNP NMR experiments, ~ 3 mg of the ground L-histidine·HCl·H$_2$O was impregnated with ~0.5 $\mu$L of a 32 mM HyTEK-2 solution in 1,1,2,2-tetrachloroethane (TCE). The powder was then transferred into a 0.7 mm zirconia rotor and

closed with vespel drive and bottom caps. A second 0.7 mm rotor was prepared with neat ground L-histidine·H$_2$O·HCl.

DNP NMR experiments were performed on a 21.2 T Bruker wide-bore NMR Avance Neo spectrometer operating at 900.14 MHz for $^1$H frequency using a 0.7 mm DNP low temperature MAS probe able to spin samples at the magic angle at rates up to 65 kHz at a temperature of about 100 K, in double resonance $^1$H–$^{13}$C configuration.[35] The probe operates in connection with to a control system providing bearing, drive, and VT N$_{2(g)}$ flows cooled to about 100 K. The MAS frequency was set to and stabilized at values between 20 kHz to 60 kHz, and spinning is typically stable to within ±9 Hz.[35] Samples were degassed using five freeze–thaw cycles prior to measurement.[37] The spectrometer is equipped with a 593 GHz gyrotron $\mu$wave source, fine-tuned to the maximum enhancement of HyTEK-2 by adjusting the cavity temperature, and producing ~15W continuous $\mu$waves at the probe base.

The $^1$H polarization build-up times in the dry (unimpregnated) materials $T_{b,dry}$ were measured using a $^1$H saturation recovery experiment. A spin echo of a total of eight rotor periods was used to remove the $^1$H probe background.

The DNP build-up times in the solvent were measured using $^1$H saturation recovery experiments followed by cross-polarization (CP) to $^{13}$C to allow $^{13}$C detection of the solvent. MAS rates from 20 to 60 kHz were used, and the experiments were performed under continuous $\mu$wave irradiation.

At each MAS rate between 20 to 60 kHz, the solvent DNP enhancements $\varepsilon_0(\omega_r)$ were measured by recording two direct $^1$H experiments, one with $\mu$wave irradiation and a second without $\mu$wave irradiation. A short spin echo (eight rotor periods) was used to remove the $^1$H probe background. The recycle delay between scans was set to 5 s. The solvent DNP enhancements were calculated by taking the ratio of the integrated $^{13}$C TCE signal with and without $\mu$waves.

The DNP enhancements of L-histidine·HCl·H$_2$O as a function of polarizing delays were measured by recording two direct $^1$H experiments, one with $\mu$wave irradiation and a second without $\mu$wave irradiation. A $^1$H spin lock at 100 kHz during 100−60 ms was used to remove the TCE solvent $^1$H signal, followed by a short spin echo (2−8 rotor periods) to avoid baseline distortions (values vary with MAS rate and more details are provided in Table S1). DNP enhancements were recorded with MAS rates from 20 kHz to 60 kHz and were calculated by taking the ratio of the integrated $^1$H signal of the secondary amine at 17 ppm with and without $\mu$waves.

Numerical simulations of R-DNP were performed using either the HPC facilities of the Scientific IT and Application Support Center of EPFL running Matlab R2019b (©Math-Works) with 28 cores (Intel Xeon 2.6 GHz) on a single calculation node with 128 GB of RAM, or an Apple Mac Pro (2019) running Matlab R2020b with 28 cores (Intel Xeon 2.5 GHz) and 192 GB RAM.

Scanning electron micrographs were performed on a Zeiss GeminiSEM300 at the EPFL CIME facility. The samples were treated with gold vapor deposition prior to analysis.

## ■ RESULTS AND DISCUSSION

**$^1$H Detected R-DNP at fast MAS.** Figure 2 shows the DNP enhanced $^1$H NMR spectra of L-histidine·HCl·H$_2$O impregnated with 32 mM HyTEK-2 in TCE at a MAS rate of 60 kHz. While the $^1$H TCE solvent signal dominates the spectrum (orange), the use of a $^1$H spin lock prior to
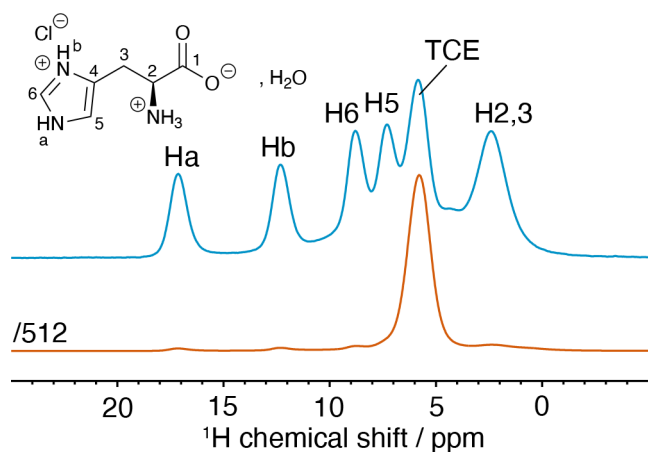
**Figure 2.** 21.2 T $^1$H DNP MAS NMR spectrum of L-histidine·HCl·H$_2$O impregnated with 32 mM HyTEK-2 in TCE, at an MAS rate of 60 kHz, recorded with (top, blue), or without (bottom, orange) TCE solvent suppression. Solvent suppression here was achieved using a 60 ms $^1$H spin-lock followed by a short $^1$H spin echo (to prevent baseline distortion).



**Figure 3.** $^1$H polarization build-up time of dry L-histidine·HCl·H$_2$O powder recorded as a function of MAS frequency, at 21.2 T and ~100 K. No significant variation of $T_{b,dry}$ was observed between the resolved $^1$H signals, thus the full $^1$H spectra was integrated to obtain the $T_{b,dry}$ at each MAS rate.

acquisition following ref 38 was found to efficiently reduce the solvent signal, and it allowed detection of well resolved $^1$H signals from the L-histidine·HCl·H$_2$O particles (blue). Such resolution, enabled by fast spinning, allowed the implement of $^1$H detected R-DNP experiments, as the $^1$H signals of L-histidine·HCl·H$_2$O, such as Ha, Hb or H2,3, can be directly integrated without the need to transfer polarization to a heteronucleus, i.e., here $^{13}$C.

**MAS Dependence of R-DNP.** We note that not only should fast MAS experiments allow access to $^1$H detected R-DNP curves but also that Prisco et al.[39] have recently highlighted the key role of $^1$H spin diffusion in MAS DNP experiments in their general approach to determining hyperpolarization transfer rates using the competitive rates of spin polarization generation, propagation, and dissipation that govern hyperpolarization transfer between large coupled spin ensembles. Since changing the MAS rate will modulate the $^1$H spin diffusion coefficient, it will lead to different relayed-DNP dynamics at different spinning rates. This in turn suggests that measuring R-DNP curves at different spinning rates will provide a set of independent data that should lead to more accurate determination of domain sizes than through the measurement of a curve at a single rate. We outline the details of this approach and provide experimental verification in the following.

**Spin–Lattice Relaxation of L-Histidine·HCl·H$_2$O.** Figure 3 shows the measured $^1$H polarization build-up time $T_{b,dry}$ recorded on a dry powder of L-histidine·HCl·H$_2$O at MAS rates from 20 kHz to 60 kHz at a sample temperature of ~100 K and at 21,15 T. $T_{b,dry}$ slowly increases from 740 to 823 s as the MAS rate increases. In the R-DNP context, the $^1$H spin–lattice relaxation time $T_1$ is defined as the build-up time of the dry spinning powder, sometime referred to as the *intrinsic* $T_1$ (*i.e.* free from $^1$H spin diffusion effects). $T_1$ in rigid organic solids, in the absence of any significant internal motion, is usually induced by random fluctuation of magnetic moments near the Larmor frequency, *i.e.*, here 900 MHz, and are usually due to the presence of paramagnetic impurities or defects in the solid that links the $^1$H spins to the thermal reservoir.[40] Spinning of the sample around the magic angle up to 60 kHz is
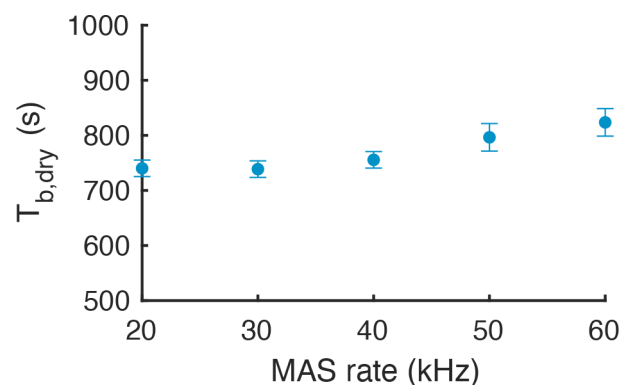
far too slow to notably interfere with the $T_1$ *intrinsic* relaxation mechanisms. Nonetheless, as shown by Kessemeier et al.,[41] $^1$H spin diffusion contributes to the *apparent* $T_1$ in solids as it connects spins to remote impurities, and thus increasing of the MAS rate decreases the $^1$H spin diffusion rate, and the *apparent* $T_1$ can increase. The weak MAS rate dependence observed for $T_{b,dry}$ can be attributed to this contribution. A potential source of impurities is oxygen absorbed into the particles.[42] Fortunately, in our sample, Figure 3 shows that $^1$H spin diffusion of sink relaxation in L-histidine·HCl·H$_2$O has minimal effect in the 20−60 kHz range. Consequently we make the following assumptions: (i) the effect of $^1$H spin diffusion on the relaxation in L-histidine·HCl·H$_2$O is negligible (ii) $T_1$ can be approximated by $T_{b,dry}$ at 60 kHz. We note that (i) is verified here for L-histidine·H$_2$O·HCl, but it might not be valid for other samples, where one might have to explicitly take into account $^1$H spin diffusion of sink relaxation in addition to the relay of hyperpolarization in the R-DNP model.

**MAS Dependence of the Diffusion Coefficient.** A key parameter for R-DNP simulations is the $^1$H spin diffusion coefficient $D$ and its dependence on the MAS frequency $\omega_r$. The exact MAS dependence of $D$ is a subject of debate. It is expected that increasing $\omega_r$ reduces $^1$H spin diffusion rate, as homonuclear dipolar couplings, the cause of spin diffusion, are progressively averaged out. Maricq and Waugh showed that in the limit of a 2-spin system treated with average Hamiltonian theory, the dipolar coupling vanishes with the inverse of $\omega_r$.[43] Nonetheless, $D$ is a multispin effect and cannot be fully described with a 2-spin system. For example, the large dipolar couplings present in a static sample could lead to homonuclear analogies of "self-decoupling" effects,[44] which can reduce the effective couplings. Slow magic angle spinning can then actually increase effective couplings, and Roos et al. made the counterintuitive observation that D in polystyrene and polyethylene actually increases at slow $\omega_r$, reaches a maximum at about $\omega_r$ = 2−3 kHz, and then decreases at faster $\omega_r$.[45] Similar observations were since made in the context of weakly magnetic nuclei.[46] Halse et al. used first-principles simulations in Liouville space to calculate $D$ for spinning solid samples of ice and L-histidine for $\omega_r$ = 5−20 kHz, and found a good fit to a $1/\omega_r$ dependence.[47] Hansen and co-workers studied $D$ between 2 and 12 kHz MAS in high density polyethylene and used the Bloembergen−Purcell−Pound equation to rationalize the dependence on $\omega_r$.[48] Since here we are exploring a much

higher spinning rate regime, between 20 to 60 kHz, we propose to extract a phenomenological MAS dependence directly from the R-DNP data.

We previously showed[29] that in the case of a solid impregnated with a polarizing solution, the steady-state DNP enhancement $\varepsilon_\infty$ is dominated by $^1H$ spin diffusion and $^1H$ spin−lattice relaxation and we derived the following formula for spherical particles:

$$\varepsilon_\infty = 1 + (\varepsilon_0 - 1)\frac{3\sqrt{DT_1}}{L}\left(\coth\left(\frac{L}{\sqrt{DT_1}}\right) - \frac{\sqrt{DT_1}}{L}\right) \quad (1)$$

where $\varepsilon_0$ is the DNP enhancement in the polarizing solution, $T_1$ is the intrinsic spin−lattice relaxation time of the solid, and L the radius of the (here spherical) solid particle. Knowing the pair $(\varepsilon_\infty, \varepsilon_0)$ for each MAS frequency, it is possible to calculate the value of $DT_1L^2$ as a function of $\omega_r$ ($(\varepsilon_\infty, \varepsilon_0)$ are given in Table S2). Figure 4 reports the value obtained for L-histidine·
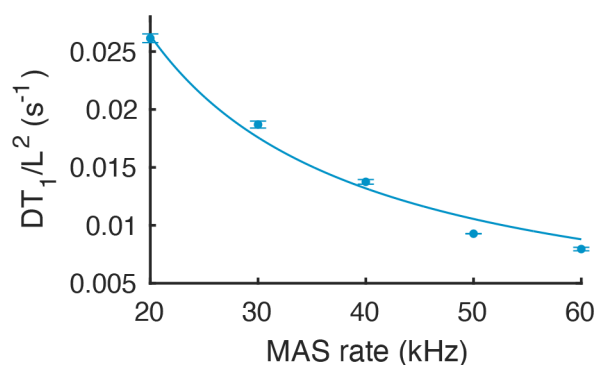


**Figure 4.** $DT_1/L^2$ as a function of the MAS rate. The dots represent the experimental values calculated from the steady-state DNP enhancement measurements on L-histidine·HCl·H$_2$O impregnated with a solution of 32 mM HyTEK-2 in TCE. The solid line shows the best fit to the data assuming that $D$ is inversely proportional to the MAS rate, and $T_1$ and $L$ are independent of MAS rate. Error bars were estimated by adding 5% random noise to $(\varepsilon_\infty, \varepsilon_0)$ and measuring the deviation of the resulting $DT_1/L^2$; this was repeated 1000 times.

HCl·H$_2$O impregnated with HyTEK-2 in TCE for $\omega_r$ between 20 and 60 kHz. As neither L nor $T_1$ depend on the MAS rate, the observed dependence is the sole consequence of the MAS dependence of $D$. We found that our experimental data are in best agreement with $D$ being inversely proportional to the MAS rate over the 20−60 kHz regime. Then, the proportionality coefficient $\widetilde{D_0}$ was obtained using the value of $D$ from Halse et al. at 5 kHz of 0.15 nm$^2$·ms$^{-1}$.[47] This leads to the following empirical dependence of the $^1H$ spin diffusion coefficient $D$ of L-histidine·HCl·H$_2$O as a function of $\omega_r$:

$$D(\omega_r) = \frac{\widetilde{D_0}}{\omega_r} \text{ with } \widetilde{D_0} = 0.75\cdot10^{-3}\mu m^2\cdot s^{-1}\cdot kHz^{-1} \quad (2)$$

**MAS Rate Modeling of R-DNP for a Single Particle Size.** Figure 5a shows the experimental DNP enhancement $\varepsilon(t)$ (data points) as a function of the polarizing time $t$ for MAS rates ranging from 20 to 60 kHz. As described in ref,[29] the $^1H$ hyperpolarization generated in the presence of $\mu$waves in the HyTEK-2/TCE phase is transported via $^1H$ spin diffusion to the L-histidine·HCl·H$_2$O particles (see Figure 1). In absence of $\mu$waves, there is still transport of polarization between the two phases since they do not have the same $^1H$
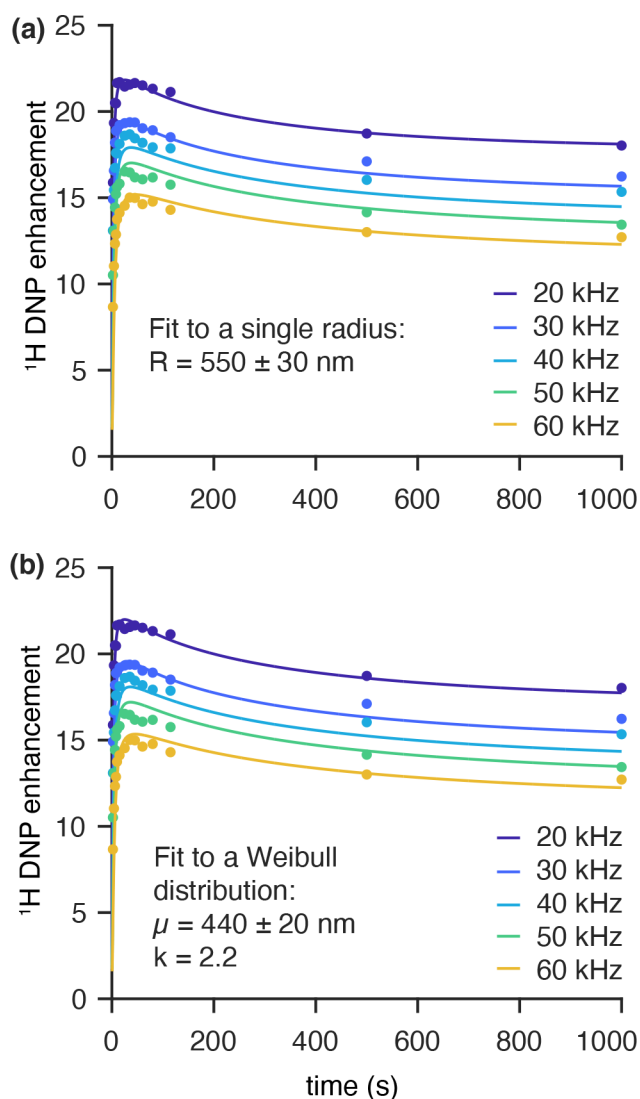


**Figure 5.** $^1H$ DNP enhancement as a function of polarization time recorded for L-histidine·HCl·H$_2$O impregnated with a solution of 32 mM HyTEK-2 in TCE. The MAS rate is varied from 20 kHz to 60 kHz. The points show the experimental data. (a) Solid lines represent the simultaneous best fit of all the data to an R-DNP model considering spherical particles of a single radius, where we find $R = 0.55 \mu m$. (b) Particle sizes are assumed to follow a Weibull distribution. The parameters found to provide the best fit (solid lines) are a scale parameter of $\mu = 0.44 \mu m$ and an order parameter of $k = 2.2$. The errors on the observed values of the steady-state enhancements are estimated to be $\pm0.08$ at 20 kHz and $\pm0.01$ at 60 kHz. The reported errors correspond to the error of the fit, they were estimated by adding 10% of random noise over the modelized $\varepsilon(t)$, measuring the deviation of the resulting fit. The process was repeated 1000 times.

build-up times and since the DNP polarizing agent induces depolarization in the HyTEK-2/TCE phase. Assuming the L-histidine·HCl·H$_2$O powder is made up of spherical particles of radius $R$, the transport of polarization can be simulated by numerically solving the $^1H$ spin diffusion equations in presence and absence of $\mu$waves. In a system with a spherical symmetry:

$$\frac{\partial P(r, t)}{\partial t} = D(\omega_r, r)\Delta P(r, t) - \frac{P(r, t) - P^0(r)}{T_1(r)} \quad (3)$$

where $P(r,t)$ is the polarization at position $r$ and time $t$; $D(\omega_r, r)$ is the $^1$H spin diffusion coefficient, which can depend on $r$ (i.e., it can vary from one phase to another) and which depends on $\omega_r$ as described above. $P^0(r)$ is the local equilibrium polarization in the absence of $^1$H spin diffusion given by

$$P^0(r) = \frac{\varepsilon_0(\omega_r)\varepsilon_{dep} + 1}{2}$$
$$+ \frac{\varepsilon_0(\omega_r)\varepsilon_{dep} - 1}{2}[\tanh(p(r - R))]: \mu w \text{ on} \tag{4}$$

$$P^0(r) = \frac{\varepsilon_{dep} + 1}{2}$$
$$+ \frac{\varepsilon_{dep} - 1}{2}[\tanh(p(r - R))]: \mu w \text{ off} \tag{5}$$

where $\varepsilon_0(\omega_r)$ is the solvent DNP enhancement measured at MAS rate $\omega_r$ and $\varepsilon_{dep} = 0.7$ is the contribution factor of HyTEK-2 (which was measured to be independent of $\omega_r$ for HyTEK-2 between 10 to 40 kHz).[36] This definition translates to, in the absence of spin diffusion, spins located in the HyTEK-2/TCE phase hyperpolarized to $\varepsilon_0(\omega_r)$ in the presence of $\mu$waves and accounts for depolarization $\varepsilon_{dep}$ in presence/absence of $\mu$waves; and that the polarization of the L-histidine·HCl·H$_2$O phase relaxes to 1.[29] $p$ is the slope the tanh function defining the separation between the two phases. $T_1(r)$ is defined as

$$T_1(r) = \frac{T_1^{hist} + T_b^{sol}(\omega_r)}{2}$$
$$+ \frac{T_1^{hist} - T_b^{sol}(\omega_r)}{2}[\tanh(p(R - r))] \tag{6}$$

where $T_1^{hist}$ is the spin−lattice relaxation time of L-histidine·HCl·H$_2$O (see discussion above); and $T_b^{sol}(\omega_r)$ is the DNP build-up time of the solvent; and $p$ is 400 $\mu$m$^{-1}$. The measured values of $\varepsilon_0(\omega_r)$ and $T_b^{sol}(\omega_r)$ are reported in the Supporting Information. The $^1$H resolution gives the possibility to calculate the L-histidine·HCl·H$_2$O enhancement as a function of time for each MAS rate:

$$\varepsilon_{\omega_r}(t) = \frac{\iiint_{V_{hist}} P_{\omega_r}^{\mu won}(r, t) \, dV_{hist}}{\iiint_{V_{hist}} P_{\omega_r}^{\mu woff}(r, t) \, dV_{hist}} \tag{7}$$

Allowing the size of the particle $R$ and the slope $p$ to vary, the full set of experimental data can be simultaneously fit, and we find that the model converges to a radius for the histidine particles of $R = 550 \pm 30$ nm. This is made with the simplified hypothesis that the powder is comprised of spherical particles of the same radius $R$.

The SEM analysis of the L-histidine·HCl·H$_2$O powder indicates that particle sizes follow a Weibull distribution centered on a radius of 374 nm with an order parameter of $k = 2.2$ as shown in Figure 6 (see Figure S1 and S2, and eq 9 for the Weibull distribution function).[49] Thus, the particle size obtained with the $^1$H detected variable MAS rate R-DNP curves up to 60 kHz appears to be in relatively good agreement with the radius obtained with SEM. Moreover, using $^1$H detection here significantly reduced the experimental time, the measurement of the DNP enhancement $\varepsilon(t)$ as a function of the polarizing time required only 4 h of signal averaging for
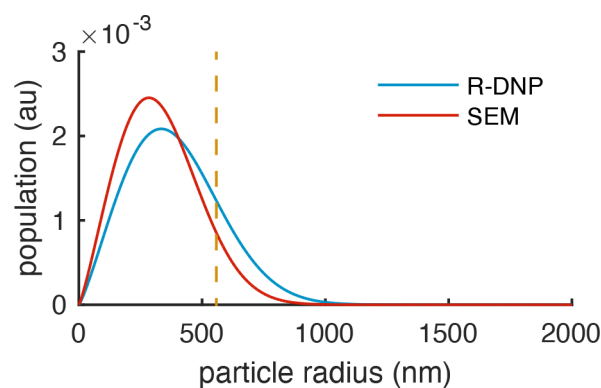


**Figure 6.** Comparison of the distributions of the particle radii determined experimentally from the R-DNP (blue) and SEM (red) measurements. The dashed orange vertical line indicates the particle radius as measured using R-DNP and if we assume only a single particle radius. Both the distributions are normalized to have an area of 1.0.

each MAS frequency (experimental times are detailed in the Supporting Information).

**MAS Rate Modeling of R-DNP with a Distribution of Particle Sizes.** Although the simplifying assumption that the L-histidine·HCl·H$_2$O powder is comprised of spherical particles of the same size yields an R-DNP particle size measurement in fairly good agreement with the SEM measurement, explicitly taking into account a particle size distribution is an obvious correction that should improve the agreement.[27] To do so, for each MAS rate, we calculated the NMR signal of spherical histidine particles with radii ranging from R = 0.05 to 5 $\mu$m in increment of 0.01 $\mu$m, with and without $\mu$wave irradiation of the sample:

$$\mathcal{S}_{\omega_r, R}^{\mu w m}(t) = \iiint_{V_{hist}(R)} P_{\omega_r, R}^{\mu w m}(t, r) \, dV_{hist}, \ m \in \{\text{on, off}\} \tag{8}$$

For a distribution of sizes in the powder, the NMR signals with $\mu$wave on/off are then calculated by summing over all the crystallites. The probability of finding a crystallite of radius $R$ is given by the particle size distribution function. Specifically, here we used a Weibull distribution:

$$g_{\mu,k}(R) = \frac{k}{\mu}\left(\frac{R}{\mu}\right)^{k-1} \exp\left(-\left(\frac{R}{\mu}\right)^k\right) \tag{9}$$

which is centered on a radius of $\mu$ (also referred to as the scale parameter) and with an order parameter $k$ and which is typically the type of distribution expected for powders formed by fragmentation or crushing[49,50] (of course, other distributions could be evaluated). The resulting DNP enhancement as a function of time can be calculated as

$$\varepsilon_{\omega_r}(t) = \frac{\sum_R g_{\mu,k}(R) \mathcal{S}_{\omega_r, R}^{\mu w on}(t)}{\sum_R g_{\mu,k}(R) \mathcal{S}_{\omega_r, R}^{\mu w off}(t)} \tag{10}$$

This treatment is similar to Rossini et al.,[27] except instead of calculating series of $\varepsilon(t)$ for each particle size, we computed a series of signals for all particle size $\mathcal{S}_{\omega_r, R}^{\mu w m}(t)$, $m \in \{\text{on, off}\}$. Figure 5b shows the results of a fit of the experimental R-DNP data fit to a fixed order parameter $k = 2.2$ (taken from the SEM) which converges to a Weibull distribution centered at $\mu = 440$ nm and shown in Figure 6. When comparing to the fit

for a single radius in Figure 5a, we see that the inclusion of the distribution makes a significant difference, and results in a more accurate measurement of the particle size. The distribution centered at $\mu$ = 440 nm is very close to the measurement performed with SEM, with the difference within the uncertainty of the SEM method to estimate the particle size distribution. Figure 6 compares the distributions determined by the SEM and R-DNP measurements and illustrates the good agreement between both.

## CONCLUSIONS

To conclude, we have first demonstrated that fast MAS (here up to 60 kHz) enables rapid acquisition of $^1$H detected R-DNP curves. With this new development in hand, we have shown how variable MAS rate R-DNP curves have different shapes, due to the modulation of $^1$H spin diffusion coefficients. We show that, not unexpectedly, $D$ scales as $1/\omega_r$ in the fast MAS regime and that a set of variable rate R-DNP curves can be modeled to obtain an accurate determination of the distribution of particle sizes present in a microcrystalline sample of L-histidine·H$_2$O·HCl.

## ASSOCIATED CONTENT

### ⓈⅠ Supporting Information

The Supporting Information is available free of charge at https://pubs.acs.org/doi/10.1021/acs.jpcc.2c01077.

> SEM image, distribution of the particle radius, $^1$H build-up curves, experimental parameters, experimental build-up times and enhancements, and detailed data deposit information (PDF)

## AUTHOR INFORMATION

### Corresponding Author

**Lyndon Emsley** − *Institut des Sciences et Ingénierie Chimiques, École Polytechnique Fédérale de Lausanne (EPFL), 1015 Lausanne, Switzerland;* ⓞ orcid.org/0000-0003-1360-2572; Email: lyndon.emsley@epfl.ch

### Authors

**Pierrick Berruyer** − *Institut des Sciences et Ingénierie Chimiques, École Polytechnique Fédérale de Lausanne (EPFL), 1015 Lausanne, Switzerland;* ⓞ orcid.org/0000-0003-1783-6034

**Andrea Bertarello** − *Institut des Sciences et Ingénierie Chimiques, École Polytechnique Fédérale de Lausanne (EPFL), 1015 Lausanne, Switzerland;* ⓞ orcid.org/0000-0003-3705-1760

**Snædís Björgvinsdóttir** − *Institut des Sciences et Ingénierie Chimiques, École Polytechnique Fédérale de Lausanne (EPFL), 1015 Lausanne, Switzerland*

**Moreno Lelli** − *Institut des Sciences et Ingénierie Chimiques, École Polytechnique Fédérale de Lausanne (EPFL), 1015 Lausanne, Switzerland; Magnetic Resonance Center (CERM) and Department of Chemistry "Ugo Schiff", University of Florence, 50019 Sesto Fiorentino, Italy*

Complete contact information is available at:
https://pubs.acs.org/10.1021/acs.jpcc.2c01077

### Author Contributions

The manuscript was written through contributions of all authors. All authors have given approval to the final version of the manuscript.

### Notes

## ACKNOWLEDGMENTS

## REFERENCES

(1) Schoenmaker, L.; Witzigmann, D.; Kulkarni, J. A.; Verbeke, R.; Kersten, G.; Jiskoot, W.; Crommelin, D. J. A. mRNA-lipid nanoparticle COVID-19 vaccines: Structure and stability. *Int. J. Pharm.* **2021**, *601*, 120586.

(2) Antimisiaris, S. G.; Marazioti, A.; Kannavou, M.; Natsaridis, E.; Gkartziou, F.; Kogkos, G.; Mourtas, S. Overcoming barriers by local drug delivery with liposomes. *Adv. Drug Deliv Rev.* **2021**, *174*, 53−86.

(3) Vishali, D. A.; Monisha, J.; Sivakamasundari, S. K.; Moses, J. A.; Anandharamakrishnan, C. Spray freeze drying: Emerging applications in drug delivery. *J. Controlled Release* **2019**, *300*, 93−101.

(4) Zhao, F. W.; Wang, C. R.; Zhan, X. W. Morphology Control in Organic Solar Cells. *Adv. Energy Mater.* **2018**, *8* (28), 1703147.

(5) Evans, H. A.; Mao, L. L.; Seshadri, R.; Cheetham, A. K. Layered Double Perovskites. *Annu. Rev. Mater. Res.* **2021**, *51*, 351−380.

(6) Peled, E.; Menkin, S. Review-SEI: Past, Present and Future. *J. Electrochem. Soc.* **2017**, *164* (7), A1703−A1719.

(7) Kong, X.; Deng, H.; Yan, F.; Kim, J.; Swisher, J. A.; Smit, B.; Yaghi, O. M.; Reimer, J. A. Mapping of functional groups in metal-organic frameworks. *Science* **2013**, *341* (6148), 882−5.

(8) Reif, B.; Ashbrook, S. E.; Emsley, L.; Hong, M. Solid-state NMR spectroscopy. *Nat. Rev. Methods Primers* **2021**, *1*, 2.

(9) Celik, G.; Kennedy, R. M.; Hackler, R. A.; Ferrandon, M.; Tennakoon, A.; Patnaik, S.; LaPointe, A. M.; Ammal, S. C.; Heyden, A.; Perras, F. A.; et al. Upcycling Single-Use Polyethylene into High-Quality Liquid Products. *ACS Cent. Sci.* **2019**, *5* (11), 1795−1803.

(10) Griffith, K. J.; Wiaderek, K. M.; Cibin, G.; Marbella, L. E.; Grey, C. P. Niobium tungsten oxides for high-rate lithium-ion energy storage. *Nature* **2018**, *559* (7715), 556−563.

(11) Jeong, J.; Kim, M.; Seo, J.; Lu, H.; Ahlawat, P.; Mishra, A.; Yang, Y.; Hope, M. A.; Eickemeyer, F. T.; Kim, M.; et al. Pseudo-halide anion engineering for alpha-FAPbI3 perovskite solar cells. *Nature* **2021**, *592* (7854), 381−385.

(12) Kang, X.; Kirui, A.; Dickwella Widanage, M. C.; Mentink-Vigier, F.; Cosgrove, D. J.; Wang, T. Lignin-polysaccharide interactions in plant secondary cell walls revealed by solid-state NMR. *Nat. Commun.* **2019**, *10* (1), 347.

(13) Kim, E. J.; Siegelman, R. L.; Jiang, H. Z. H.; Forse, A. C.; Lee, J. H.; Martell, J. D.; Milner, P. J.; Falkowski, J. M.; Neaton, J. B.; Reimer, J. A.; et al. Cooperative carbon capture and steam regeneration with tetraamine-appended metal-organic frameworks. *Science* **2020**, *369* (6502), 392−396.

(14) Kubicki, D. J.; Stranks, S. D.; Grey, C. P.; Emsley, L. NMR spectroscopy probes microstructure, dynamics and doping of metal halide perovskites. *Nat. Rev. Chem.* **2021**, *5* (9), 624−645.

(15) Lee, M.; Wang, T.; Makhlynets, O. V.; Wu, Y.; Polizzi, N. F.; Wu, H.; Gosavi, P. M.; Stohr, J.; Korendovych, I. V.; DeGrado, W. F.; et al. Zinc-binding structure of a catalytic amyloid from solid-state NMR. *Proc. Natl. Acad. Sci. U. S. A.* **2017**, *114* (24), 6191−6196.

(16) Mandala, V. S.; McKay, M. J.; Shcherbakov, A. A.; Dregni, A. J.; Kolocouris, A.; Hong, M. Structure and drug binding of the SARS-CoV-2 envelope protein transmembrane domain in lipid bilayers. *Nat. Struct Mol. Biol.* **2020**, *27* (12), 1202−1208.

(17) Schmidt-Rohr, K.; Spiess, H. W. *Multidimensional solid-state NMR and polymers*; Academic Press: London and San Diego, CA, 1994.

(18) Terrett, O. M.; Lyczakowski, J. J.; Yu, L.; Iuga, D.; Franks, W. T.; Brown, S. P.; Dupree, R.; Dupree, P. Molecular architecture of softwood revealed by solid-state NMR. *Nat. Commun.* 2019, 10 (1), 4978.

(19) Walkley, B.; Provis, J. L. Solid-state nuclear magnetic resonance spectroscopy of cements. *Mater. Today Adv.* 2019, 1, 100007.

(20) Cordova, M.; Balodis, M.; Hofstetter, A.; Paruzzo, F.; Nilsson Lill, S. O.; Eriksson, E. S. E.; Berruyer, P.; Simões de Almeida, B.; Quayle, M. J.; Norberg, S. T.; et al. Structure determination of an amorphous drug through large-scale NMR predictions. *Nat. Commun.* 2021, 12 (1), 2964.

(21) Clauss, J.; Schmidt-Rohr, K.; Spiess, H. W. Determination of Domain Sizes in Heterogeneous Polymers by Solid-State Nmr. *Acta Polym.* 1993, 44 (1), 1−17.

(22) Schmidt-Rohr, K.; Clauss, J.; Spiess, H. W. Correlation of Structure, Mobility, and Morphological Information in Heterogeneous Polymer Materials by 2-Dimensional Wideline-Separation Nmr-Spectroscopy. *Macromolecules* 1992, 25 (12), 3273−3277.

(23) Schmidt-Rohr, K.; Clauss, J.; Blumich, B.; Spiess, H. W. Miscibility of Polymer Blends Investigated by H-1 Spin Diffusion and C-13 Nmr Detection. *Magn. Reson. Chem.* 1990, 28, S3−S9.

(24) Kundu, K.; Mentink-Vigier, F.; Feintuch, A.; Vega, S. DNP Mechanisms. *eMagRes* 2019, 8 (3), 295−337.

(25) Maly, T.; Debelouchina, G. T.; Bajaj, V. S.; Hu, K. N.; Joo, C. G.; Mak-Jurkauskas, M. L.; Sirigiri, J. R.; van der Wel, P. C.; Herzfeld, J.; Temkin, R. J.; et al. Dynamic nuclear polarization at high magnetic fields. *J. Chem. Phys.* 2008, 128 (5), 052211.

(26) Lesage, A.; Lelli, M.; Gajan, D.; Caporini, M. A.; Vitzthum, V.; Mieville, P.; Alauzun, J.; Roussey, A.; Thieuleux, C.; Mehdi, A.; et al. Surface enhanced NMR spectroscopy by dynamic nuclear polarization. *J. Am. Chem. Soc.* 2010, 132 (44), 15459−61.

(27) Rossini, A. J.; Zagdoun, A.; Hegner, F.; Schwarzwalder, M.; Gajan, D.; Coperet, C.; Lesage, A.; Emsley, L. Dynamic nuclear polarization NMR spectroscopy of microcrystalline solids. *J. Am. Chem. Soc.* 2012, 134 (40), 16899−908.

(28) van der Wel, P. C.; Lewandowski, J. R.; Griffin, R. G. Solid-state NMR study of amyloid nanocrystals and fibrils formed by the peptide GNNQQNY from yeast prion protein Sup35p. *J. Am. Chem. Soc.* 2007, 129 (16), 5117−30.

(29) Pinon, A. C.; Schlagnitweit, J.; Berruyer, P.; Rossini, A. J.; Lelli, M.; Socie, E.; Tang, M. X.; Pham, T.; Lesage, A.; Schantz, S.; et al. Measuring Nano- to Microstructures from Relayed Dynamic Nuclear Polarization NMR. *J. Phys. Chem. C* 2017, 121 (29), 15993−16005.

(30) Viger-Gravel, J.; Schantz, A.; Pinon, A. C.; Rossini, A. J.; Schantz, S.; Emsley, L. Structure of Lipid Nanoparticles Containing siRNA or mRNA by Dynamic Nuclear Polarization-Enhanced NMR Spectroscopy. *J. Phys. Chem. B* 2018, 122 (7), 2073−2081.

(31) Viger-Gravel, J.; Lan, W.; Pinon, A. C.; Berruyer, P.; Emsley, L.; Bardet, M.; Luterbacher, J. Topology of Pretreated Wood Fibers Using Dynamic Nuclear Polarization. *J. Phys. Chem. C* 2019, 123 (50), 30407−30415.

(32) Pinon, A. C.; Skantze, U.; Viger-Gravel, J.; Schantz, S.; Emsley, L. Core-Shell Structure of Organic Crystalline Nanoparticles Determined by Relayed Dynamic Nuclear Polarization NMR. *J. Phys. Chem. A* 2018, 122 (44), 8802−8807.

(33) Viger-Gravel, J.; Pinon, A. C.; Bjorgvinsdottir, S.; Skantze, U.; Svensk Ankarberg, A.; Von Corswant, C.; Schantz, S.; Emsley, L. High Sensitivity Detection of a Solubility Limiting Surface Transformation of Drug Particles by DNP SENS. *J. Pharm. Sci.* 2021, 110 (6), 2452−2456.

(34) Berruyer, P.; Moutzouri, P.; Gericke, M.; Jakobi, D. r.; Bardet, M.; Heinze, T.; Karlson, L.; Schantz, S.; Emsley, L. Spatial Distribution of Functional Groups in Cellulose Ethers by DNP-Enhanced Solid-State NMR Spectroscopy. *Macromolecules* 2022, DOI: 10.1021/acs.macromol.2c00061.

(35) Berruyer, P.; Bjorgvinsdottir, S.; Bertarello, A.; Stevanato, G.; Rao, Y.; Karthikeyan, G.; Casano, G.; Ouari, O.; Lelli, M.; Reiter, C.; et al. Dynamic Nuclear Polarization Enhancement of 200 at 21.15 T Enabled by 65 kHz Magic Angle Spinning. *J. Phys. Chem. Lett.* 2020, 11 (19), 8386−8391.

(36) Wisser, D.; Karthikeyan, G.; Lund, A.; Casano, G.; Karoui, H.; Yulikov, M.; Menzildjian, G.; Pinon, A. C.; Purea, A.; Engelke, F.; et al. BDPA-Nitroxide Biradicals Tailored for Efficient Dynamic Nuclear Polarization Enhanced Solid-State NMR at Magnetic Fields up to 21.1 T. *J. Am. Chem. Soc.* 2018, 140 (41), 13340−13349.

(37) Kubicki, D. J.; Rossini, A. J.; Purea, A.; Zagdoun, A.; Ouari, O.; Tordo, P.; Engelke, F.; Lesage, A.; Emsley, L. Amplifying dynamic nuclear polarization of frozen solutions by incorporating dielectric particles. *J. Am. Chem. Soc.* 2014, 136 (44), 15711−8.

(38) Yarava, J. R.; Chaudhari, S. R.; Rossini, A. J.; Lesage, A.; Emsley, L. Solvent suppression in DNP enhanced solid state NMR. *J. Magn. Reson.* 2017, 277, 149−153.

(39) Prisco, N. A.; Pinon, A. C.; Emsley, L.; Chmelka, B. F. Scaling analyses for hyperpolarization transfer across a spin-diffusion barrier and into bulk solid media. *Phys. Chem. Chem. Phys.* 2021, 23 (2), 1006−1020.

(40) Bloembergen, N. On the Interaction of Nuclear Spins in a Crystalline Lattice. *Physica* 1949, 15 (3−4), 386−426.

(41) Kessemeier, H.; Norberg, R. E. Pulsed Nuclear Magnetic Resonance in Rotating Solids. *Phys. Rev.* 1967, 155 (2), 321.

(42) Rossini, A. J.; Zagdoun, A.; Lelli, M.; Gajan, D.; Rascon, F.; Rosay, M.; Maas, W. E.; Coperet, C.; Lesage, A.; Emsley, L. One hundred fold overall sensitivity enhancements for Silicon-29 NMR spectroscopy of surfaces by dynamic nuclear polarization with CPMG acquisition. *Chem. Sci.* 2012, 3 (1), 108−115.

(43) Maricq, M. M.; Waugh, J. S. Nmr in Rotating Solids. *J. Chem. Phys.* 1979, 70 (7), 3300−3316.

(44) Mehring, M. *Principles of High Resolution NMR in Solids*: Springer: Berlin and Heidelberg, Germany, 1983.

(45) Roos, M.; Micke, P.; Saalwachter, K.; Hempel, G. Moderate MAS enhances local (1)H spin exchange and spin diffusion. *J. Magn. Reson.* 2015, 260, 28−37.

(46) Bjorgvinsdottir, S.; Walder, B. J.; Matthey, N.; Emsley, L. Maximizing nuclear hyperpolarization in pulse cooling under MAS. *J. Magn. Reson.* 2019, 300, 142−148.

(47) Halse, M. E.; Zagdoun, A.; Dumez, J. N.; Emsley, L. Macroscopic nuclear spin diffusion constants of rotating polycrystalline solids from first-principles simulation. *J. Magn. Reson.* 2015, 254, 48−55.

(48) Jia, Z.; Zhang, L.; Chen, Q.; Hansen, E. W. Proton spin diffusion in polyethylene as a function of magic-angle spinning rate. A phenomenological approach. *J. Phys. Chem. A* 2008, 112 (6), 1228−33.

(49) Tenchov, B. G.; Yanev, T. K. Weibull Distribution of Particle Sizes Obtained by Uniform Random Fragmentation. *J. Colloid Interface Sci.* 1986, 111 (1), 1−7.

(50) Rosin, P.; Rammler, E. The Laws Governing the Fineness of powdered coal. *Journal of the Institute of Fuel* 1933, 7, 29−36.